Study on transition to turbulence of rotating-disk boundary layer in a rotor-stator cavity with temperature gradient

Qiang Du [*] [,*] Yaguang Xie,[†] and Lei Xie
Institute of Engineering Thermophysics, Chinese Academy of Sciences, 100190 Beijing, China;
Key Lab of Light-duty Gas-turbine, Chinese Academy of Sciences, 100190 Beijing, China;
and University of Chinese Academy of Sciences, 100049 Beijing, China

Ruonan Wang [*]
Faculty of Engineering and Physical Sciences, University of Surrey, Guildford, GU2 7XH, United Kingdom

A comprehensive approach, combining theoretical analysis and large-eddy simulation, is employed in this study to investigate the influence of temperature gradient on the stability phenomenon of the von Kármán boundary layer in a rotor-stator cavity. Further from previous studies, a temperature term is introduced to account for centrifugal buoyancy within the cavity. The focus is on analyzing the transitional behavior and the effects of centrifugal buoyancy on the boundary layer of the rotating disk under operating conditions characterized by a Reynolds number $\mathrm{Re} = \Omega_D b^2/\nu = 4 \times 10^5$. The findings highlight that a temperature gradient between the stationary and rotating disks establishes enhanced flow circulation within the cavity. Consequently, this temperature gradient significantly influences the base flow and alters the critical Reynolds numbers governing the rotating-disk boundary layer transition. Specifically, in the rotating-disk boundary layer, centrifugal buoyancy causes the premature breakdown of some inviscid modes, leading to an earlier transition to turbulence at lower Reynolds numbers. However, there exists a minimum critical Reynolds number in the rotating-disk boundary layer, beyond which the increase in centrifugal buoyancy does not further reduce the critical Reynolds number. This research emphasizes the importance of considering temperature variations in rotor-stator cavities for improved control of the stability within the rotating-disk boundary layer flow.

I. INTRODUCTION

Since von Kármán's [1] seminal work in 1921, the flow on a single rotating disk has been extensively studied. However, Alfredsson *et al.* [2] highlighted in his review that there are still many unresolved issues regarding the stability of boundary layer flow on rotating disks. When we shift our focus to a rotor-stator cavity found in aero engines, the presence of inevitable temperature differences between the rotating and stationary disks introduces even more unpredictable stability concerns on the rotating-disk boundary layer flow (referred to as the von Kármán boundary layer for an infinitely large rotating disk). Building upon existing research on the rotating-disk boundary layer flow, this study aims to investigate how temperature differences affect the characteristics of laminar-transition-turbulent flow in the boundary layer on the rotating side at high Reynolds number.

The most common flow configuration in the rotor-stator cavity is known as the Batchelor flow [3]. The main characteristic of this flow is that there is the centrifugal on rotating-disk boundary

---

*Corresponding author: duqiang@iet.cn
†Corresponding author: xieyaguang@iet.cn

layer, and the centripetal on stationary-disk boundary later, which are separated by a central rotating core.

Under the pump effect, the fluid in the rotating-disk boundary layer moves from the low radial region to the high radial region, accompanied by an increase in the local rotational Reynolds number $\text{Re}_r = \Omega_D r^2/\nu$, where Ω_D represents the rotational speed of the disk, r refers to the local radial position, and ν denotes dynamic viscosity (see Appendix for a full list of the nomenclature). Notably, in this paper, the superscript $*$ denotes dimensional physical quantities. Conversely, parameters without a superscript $*$ are dimensionless. When the flow becomes unstable at a certain radial position, as it flows radially outward, a transition from laminar to turbulent flow occurs. However, due to its ease of capturing the transition from instability to turbulence, the pathway of transition to turbulence on the rotating-disk boundary layer has also been extensively studied [4,5].

The early research on the rotating-disk boundary layer was primarily focused on theoretical and experimental investigations. Kobayashi *et al.* [6] and Malik *et al.* [7] using hot-wire anemometry both gave the Reynolds number R ($R = r/\delta$, $\delta = \sqrt{\nu/\Omega_D}$ is the characteristic viscous length) for the onset of convective instability for stationary spiral waves mode slightly below 300. Through visualizations of the transition regime by using close-up camera, Kohama [8] discovered that the phase velocity of the vortices is zero, indicating that the vortices remain stationary relative to the disk. Lingwood [9] defined the spiral waves mode as Type I instabilities through linear stability analysis, encompassing both stationary and traveling spiral waves. These instabilities are induced by velocity inflection points and belong to inviscid crossflow instabilities. Conversely, another type of instability, characterized by circular waves appearing in the disk boundary layer, was defined as a Type II instability, arising from the interaction between viscosity and Coriolis forces. In addition, Lingwood [9,10] discovered a Type III instability mode combines with the Type I instability above $R = 507$ to form an absolute instability regime, inducing nonlinear effects that mark the onset of turbulent transition. She also confirmed experimentally [11] the absolute instability above 507 by introducing a traveling wave packet into the boundary layer and observing that the trailing edge becomes fixed (radially) in space as it approaches $R = 507$, resulting in a fully turbulent flow at about $R = 600$–650. Pier's [12] theoretical research indicated that a global nonlinear elephant mode may exist at the onset of local absolute instability, while numerical solutions of linearized Navier–Stokes equations [13,14] and the experimental investigation of Othman and Corke [15] using a low-amplitude initial pulse-jet excitation demonstrated that a convective behavior eventually dominates even though regions of strong local absolute instability were present in the flow, therefore demonstrating its linear global stability. The existence of global nonlinear modes while the flow remains globally linearly stable implies the presence of subcritical global bifurcations. Appelquist *et al.* [16] demonstrated this phenomenon using linearized direct numerical simulation (DNS) in a rotating disk. Recently, Lee *et al.* [17] made a significant discovery, indicating that the vibration source responsible for the growth of velocity fluctuations through global instability lies in the range $R = 611$ to $R = 630$. This finding highlights the need for further investigation into the transition mechanism of the von Kármán boundary layer to turbulence.

Recently, there has been a growing interest in studying the laminar-transition-turbulent process in the rotating-disk boundary layer on the rotating side under more complex influencing factors. Viaud *et al.* [18] studied the laminar-transition-turbulent problem in an open cavity between two rotating disks using DNS. They confirmed the correctness of Pier [12] and demonstrated that nonparallel effects counteract the absolute instability and restore the flow stability. Viaud *et al.* [19] also studied the stability of the elephant mode by extending the cavity in both radial and azimuthal directions. They found that, when the Reynolds number was increased beyond the critical value at which nonlinear global modes and extra-large amplitude pulse disturbances led to a globally unstable self-sustaining wave, which resulted in a highly disordered state and triggered the transition to turbulence. This was the first confirmation of the possibility of direct bypass transition from elephant mode to turbulence through secondary instability in practical flow. Yim *et al.* [20] using a rotor-stator cavity to investigate the transition to turbulence on the rotating-disk boundary layer. They pointed out that, at higher Reynolds numbers, the wave forms a steep front that is no longer driven by
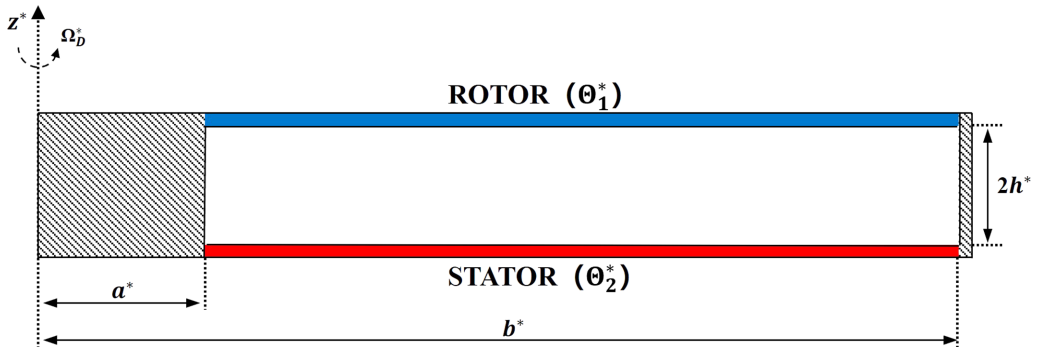
FIG. 1. Sketch of the computational domain for stator-rotor cavity flow. Ω_D^* is the angular velocity, $2h^*$ is distance between stator and rotor, and a^* and b^* are the radii of the hub and shroud surface, respectively. The rotor is rotating with the hub, while the shroud and stator are motionless.

the edge, and then generates saturated spiral waves downstream, ultimately leading to the onset of turbulence.

This study specifically focuses on a higher rotational Reynolds number, $\mathrm{Re} = \Omega_D b^2/\nu = 4 \times 10^5$, where b represents the maximum radius of the disk. It presents a comprehensive analysis of the impact of temperature-induced centrifugal buoyancy on the rotating-disk boundary layer within the rotor-stator cavity. In fact, the relationship between the vertical temperature gradient between a high-temperature stationary disk and a low-temperature rotating disk and the direction of centrifugal force has been extensively discussed in the field of thermal convection [21–23]. Expanding the range of factors influencing the stability of the rotating-disk boundary layer not only deepens our understanding of flow dynamics but also offers valuable insights for predicting the flow behavior within the rotor-stator cavity under varying temperature gradients.

To facilitate a comprehensive and logically sound investigation of the aforementioned research topics and build on existing research on the rotating-disk boundary layer without temperature difference, we use a combination of theoretical analysis, large-eddy simulations (LESs), and linear stability analyses (LSAs) to carefully examine the influence of temperature on the boundary layer.

This paper is organized as follows: in Sec. II the setup of the simulation is described, including the geometrical, mathematical, and numerical modeling. Sections III and IV presents an extended study of the problem within the von Kármán boundary layer through Bödewadt-Ekman-von Kármán (BEK) model and large-eddy simulation. Section V provide insights into the effects of temperature gradients on the base flow within the BEK model and the variations in the temporal growth rate induced by the base flow in the analysis of local linear stability, respectively. Finally, conclusions are provided and we discuss our future work on the problem of laminar-turbulent transition.

II. PROBLEM FORMULATION

A. Geometry

In this study, the geometric model follows the configuration used in previous works by Séverac *et al.* [24], Poncet and Serre [25], Queguineur *et al.* [26], and Du *et al.* [27], a section of which is shown in Fig. 1. It consists of an enclosed annulus with a radial extent of $b^* - a^*$, where a^* and b^* are the internal and external radii, respectively. The distance between the two disks is $2h^*$. The stator is connected to the external cylinder, while the rotor is connected to the internal cylinder, rotating around the z axis at an angular velocity of Ω_D^*. The geometry is characterized by two fixed parameters: the curvature parameter $Rm = (b^* + a^*)/(b^* - a^*)$ and the aspect ratio $L = (b^* - a^*)/2h^*$, which are set to 1.8 and 5, respectively.

TABLE I. Computational parameters used in the simulations. Re is the global Reynolds number, $\beta\Delta\Theta$ is the thermal Rossby number B, δt is the time step used for each iteration, where T is the rotational period of the disk. N_z, N_r, N_θ are the number of mesh nodes in the axial, radial, and circumferential directions, respectively.

	Stator	Rotor	Re	$\beta\Delta\Theta$	δt	N_z	N_r	N_θ
Case1	Turbulent	Laminar-transition-turbulent	4×10^5	0	$T/62800$	157	523	384
Case2	Turbulent	Laminar-transition-turbulent	4×10^5	0.05	$T/62800$	157	523	384
Case3	Turbulent	Laminar-transition-turbulent	4×10^5	0.1	$T/62800$	157	523	384

B. Mathematical

The study solves the incompressible Navier-Stokes equations for flow in cylindrical coordinate system rotating with angular velocity Ω_D, considering five variables (W, U, V, Θ, P). To achieve nondimensionalization, length, time, and velocity terms are scaled using h^*, Ω_D^{*-1}, and $\Omega_D^* h^*$, respectively. The dimensionless temperature Θ is defined as $\Theta = (2\Theta^* - \Theta_2^* - \Theta_1^*)/(\Theta_2^* - \Theta_1^*)$, where Θ_1^* represents the temperature on the rotor, and Θ_2^* is the temperature on the stator. The global Reynolds number is defined as $\text{Re} = \Omega_D b^2/\nu$ to control the flow. In this study, the typical Reynolds numbers $\text{Re} = 4 \times 10^5$ is selected, with detailed parameter settings provided in Table I. The choice of $\text{Re} = 4 \times 10^5$ aims to investigate the effect of the thermal Rossby number [$B = \beta^*(\Theta_2 - \Theta_1)$, where $\beta^* = 1/\Theta_{\text{ref}}^*$ and $\Theta_{\text{ref}}^* = (\Theta_2^* + \Theta_1^*)/2$]. This represents a typical Reynolds number where laminar, transitional, and turbulent flows coexist in the rotating-disk boundary layer. The flow characteristics of this case can be found in the literature [9,10,20,28–30]. Therefore, these Reynolds numbers are suitable for investigating the effect of the thermal Rossby number on the transition process.

Lingwood [10] defined the Rossby (Ro) and local Reynolds (Re_δ) numbers to reflect the local stability:

$$\text{Ro}(r) = \Delta\Omega(r)/\Omega(r), \quad \text{Re}_\delta(r) = \text{Ro}(r)\frac{r}{\delta}, \tag{1}$$

where $\Delta\Omega(r) = \Omega_F(r) - \Omega_D$, $\Omega_F(r)$ represents the rotational velocity of the fluid, and r denotes the dimensional radius r^*/h^*. δ is the characteristic viscous length and $\Omega(r)$ is a reference rotation rate of the system:

$$\delta = \sqrt{\nu/\Omega(r)}, \tag{2}$$

$$\Omega(r) = [\Omega_F(r) + \Omega_D]/4 + \sqrt{\{[\Omega_F(r) + \Omega_D]/4\}^2 + [\Omega_F(r) - \Omega_D]^2/2}. \tag{3}$$

For a single rotating disk, $\Omega_F(r)$ represents the rotational velocity of the fluid away from the disk boundary layer so that $\Omega_F = 0$. In a rotor-stator cavity, $\Omega_F(r)$ is commonly defined as the rotational velocity of the vortex core in the Batchelor flow [3].

In the simulation, to address the singularity issue of the velocity component V at the two junctions, one connecting the stationary shroud and the rotating disk, and the other one connecting the rotating hub and stator. The summary of boundary conditions is as follows:

$$U = 0, \quad V = \Omega_D r, \quad W = 0, \quad \Theta = \Theta_1, \quad \text{rotor},$$

$$U = 0, \quad V = 0, \quad W = 0, \quad \Theta = \Theta_2, \quad \text{stator},$$

$$U = 0, \quad V = \Omega_D a\{1 - \exp[-(1 + x/h)/0.006]\}, \quad W = 0, \quad \partial\Theta/\partial r = 0, \quad \text{hub},$$

$$U = 0, \quad V = \Omega_D b \exp[(x/h - 1)/0.006], \quad W = 0, \quad \partial\Theta/\partial r = 0, \quad \text{shroud}, \tag{4}$$

where the value 0.006 was shown to accurately model the velocity profiles observed in experiments [31].

C. Large-eddy simulation based on entropy-viscosity method

Due to the high Reynolds number, in order to reduce computational costs, we have chosen to employ the large-eddy simulation entropy viscosity method (LES-EVM). This method proposed by Guermond [32] and Guermond *et al.* [33,34] utilizes the concept of the entropy residual. In the study conducted by Wang *et al.* [35] and Du *et al.* [27], parameters α_E and β_E were introduced for enhancing the controllable flow field stability, and an implicit temperature implementation method was incorporated into the LES-EVM. The capability of obtaining high-fidelity flow fields using the proposed model was validated through verification with the open-source code SEMTEX [36].

To employ the Boussinesq approximation, the governing equations are expressed in a cylindrical coordinate system rotating with angular velocity Ω_D,

$$\frac{\partial \boldsymbol{u}}{\partial t} + \boldsymbol{N}(\boldsymbol{u}) = -\frac{\boldsymbol{\nabla}P}{\rho} + \nu\nabla^2\boldsymbol{u} - 2\Omega_D \times \boldsymbol{u} + \beta(\Theta - \Theta_{\text{ref}})\Omega_D \times (\Omega_D \times r) + \boldsymbol{\nabla} \cdot (\nu_E\boldsymbol{\nabla}\boldsymbol{u}), \quad (5)$$

$$\boldsymbol{\nabla} \cdot \boldsymbol{u} = 0, \quad (6)$$

$$\frac{\partial \Theta}{\partial t} + \boldsymbol{u} \cdot \boldsymbol{\nabla}\Theta = \kappa\nabla^2\Theta + \boldsymbol{\nabla} \cdot (\nu_\Theta\boldsymbol{\nabla}\Theta). \quad (7)$$

where $\boldsymbol{u} = \boldsymbol{u}(r, \theta, z, t) = (U, V, W)(t)$ is the velocity field, and $\boldsymbol{N}(\boldsymbol{u})$ represents nonlinear advection terms. Here we consider the nonlinear term in skew-symmetric form $\boldsymbol{N}(\boldsymbol{u}) = (\boldsymbol{u} \cdot \boldsymbol{\nabla}\boldsymbol{u} + \boldsymbol{\nabla} \cdot \boldsymbol{u}\boldsymbol{u})/2$. P is the pressure, ρ is the density, and ν is the kinematic viscosity of fluid. The variables r, θ, z, and t represent, the radial, azimuthal, axial, and time coordinates, respectively. ν_E and ν_Θ are two scalars denoting the turbulent eddy viscosity and turbulent diffusivity. For more specific details, please refer to Du *et al.* [27].

The mesh is based on $N_r \times N_z$ Gauss–Lobatto collocation points in the meridional (r, z) semiplane and Fourier expansions in the azimuthal direction and we used a fifth-order polynomial so that $(N_z \times N_r \times N_\theta) = (157 \times 523 \times 384)$ and $N_{\text{nel}} = 31.53$ million. The current grid is sufficiently refined to capture the flow characteristics within the boundary layer, as compared with the grids used by Séverac *et al.* [24] ($N_{\text{nel}} = 2.85$ million) and Yim *et al.* [20] ($N_{\text{nel}} = 5.78$ million) at the same Reynolds number. The time step for each iteration is $T/62\,800$. By utilizing 192 CPUs, one step could be completed in three seconds. To further validate the accuracy of our model and grid, we compared the results of case 1 with the experiments conducted by Séverac *et al.* [24]. Figures 2(a)–2(d) compare the average radial velocity, azimuthal velocity, root-mean-square of radial velocity, and root-mean-square of azimuthal velocity, respectively. Based on the comparisons with the experimental data, it can be concluded that the current model and grid are adequate.

III. THEORETICAL MODEL FOR VON KÁRMÁN FLOW UNDER NONISOTHERMAL FLOW

The BEK model describes a family of boundary-layer flows caused by a differential rotation rate between a solid boundary, or disk, and an incompressible fluid in rigid-body rotation above. The typical boundary layers in the BEK system are the Ekman, von Kármán, and Bödewadt boundary layers, where the von Kármán and Bödewadt boundary layers correspond to the boundary layers on the rotating and stationary sides of the rotor-stator cavity, respectively. In recent years, many researchers have made appropriate modifications to the BEK model, such as incorporating partial slip boundary conditions, to investigate the influence of surface roughness on the stability of the BEK model [37–39]. In this section, we derive the BEK model in the cylindrical coordinate (r^*, θ^*, z^*) system rotating at an angular velocity Ω_D^*. We add the temperature diffusion equation and the centrifugal buoyancy force to solve the system of differential
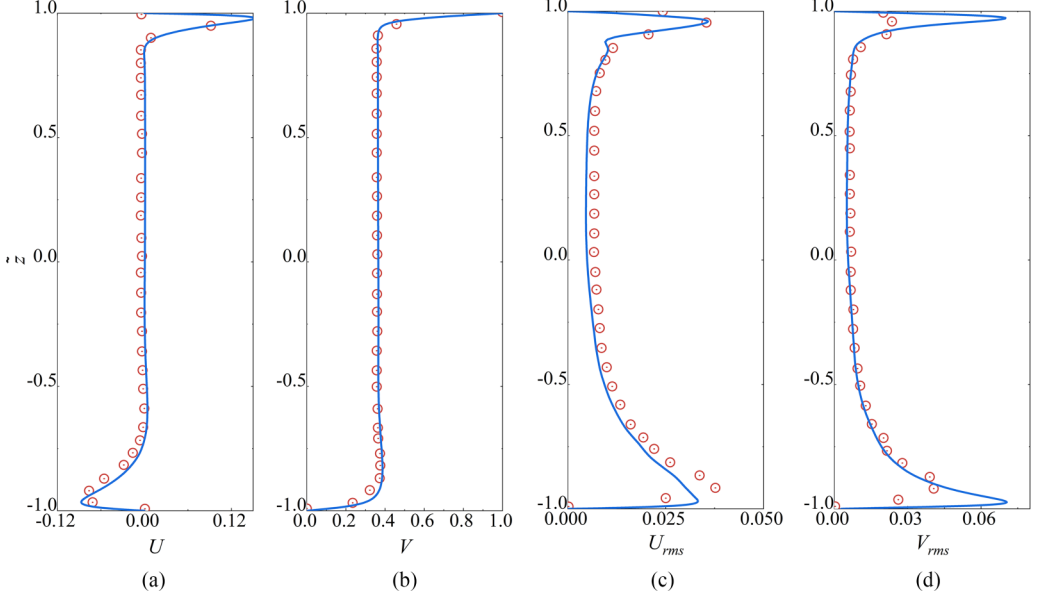
FIG. 2. The dimensionless average (a) radial velocity, (b) azimuthal velocity, (c) root-mean-square (rms) radial velocity, and (d) root-mean-square (rms) azimuthal velocity corresponding to case 1 (blue line) and experimental (red circle).

equations

$$\frac{1}{r^*}\frac{\partial(r^*U^*)}{\partial r^*} + \frac{\partial W^*}{\partial z^*} = 0, \tag{8}$$

$$U^*\frac{\partial U^*}{\partial r^*} + W^*\frac{\partial U^*}{\partial z^*} - \frac{V^{*2}}{r^*} - 2\Omega_d^* V^* = -\frac{1}{\rho^*}\frac{\partial P^*}{\partial r^*} + \left(1 - \frac{\Theta^* - \Theta_1^*}{\Theta_{\mathrm{ref}}^*}\right)\Omega_d^{*2}r^*$$
$$+ \nu^*\left[\frac{1}{r^*}\frac{\partial}{\partial r^*}\left(r^*\frac{\partial U^*}{\partial r^*}\right) + \frac{\partial^2 U^*}{\partial z^{*2}} - \frac{U^*}{r^{*2}}\right], \tag{9}$$

$$U^*\frac{\partial V^*}{\partial r^*} + W^*\frac{\partial V^*}{\partial z^*} + \frac{U^*V^*}{r^*} + 2\Omega_d^* U^* = \nu^*\left[\frac{1}{r^*}\frac{\partial}{\partial r^*}\left(r^*\frac{\partial V^*}{\partial r^*}\right) + \frac{\partial^2 V^*}{\partial z^{*2}} - \frac{V^*}{r^{*2}}\right], \tag{10}$$

$$U^*\frac{\partial W^*}{\partial r^*} + W^*\frac{\partial W^*}{\partial z^*} = -\frac{1}{\rho^*}\frac{\partial P^*}{\partial \mathrm{x}^*} + \nu^*\left[\frac{1}{r^*}\frac{\partial}{\partial r^*}\left(r^*\frac{\partial W^*}{\partial r^*}\right) + \frac{\partial^2 W^*}{\partial \mathrm{z}^{*2}}\right], \tag{11}$$

$$U^*\frac{\partial \Theta^*}{\partial r^*} + W^*\frac{\partial \Theta^*}{\partial z^*} = \alpha^*\left[\frac{1}{r^*}\frac{\partial}{\partial r^*}\left(r^*\frac{\partial \Theta^*}{\partial r^*}\right) + \frac{\partial^2 \Theta^*}{\partial \mathrm{z}^{*2}}\right], \tag{12}$$

where $[U^*, V^*, W^*, \Theta^*, P^*]$ denotes the mean radial velocity, azimuthal velocity, axial velocity, temperature, and pressure. Assuming L^* is dimensionless length, U_{ref}^* is dimensionless velocity, so $(U^*, V^*, W^*) = (U, V, \delta W)U_{\mathrm{ref}}^*$, $(r^*, z^*) = (r, \delta x)L^*$, and $P = P^*\rho^*U_{\mathrm{ref}}^*$. The temperature $\Theta = (\Theta^* - \Theta_1^*)/(\Theta_2^* - \Theta_1^*)$, where $\Theta_{\mathrm{ref}}^* = \Theta_1^*$, Using the Boussinesq assumption, it can be shown that $\beta = 1/\Theta_{\mathrm{ref}}^*$.

Equations (8)–(12) can be simplified as

$$\frac{1}{r}\frac{\partial(rU)}{\partial r} + \frac{\partial W}{\partial z} = 0, \tag{13}$$

$$U \frac{\partial U}{\partial r} + W \frac{\partial U}{\partial z} - \frac{V^2}{r} - 2V = -\frac{1}{\text{Re}} \frac{\partial P}{\partial r} + (1 - \beta\Theta)r + \frac{1}{\delta^2 \text{Re}} \frac{\partial^2 U}{\partial z^2}, \tag{14}$$

$$U \frac{\partial V}{\partial r} + W \frac{\partial V}{\partial z} + \frac{UV}{r} + 2U = \frac{1}{\delta^2 \text{Re}} \frac{\partial^2 V}{\partial z^2}, \tag{15}$$

$$U \frac{\partial W}{\partial r} + W \frac{\partial W}{\partial z} = -\frac{1}{\delta^2} \frac{\partial P}{\partial z} + \frac{1}{\delta^2 \text{Re}} \frac{\partial^2 W}{\partial z^2}, \tag{16}$$

$$U \frac{\partial \Theta}{\partial r} + W \frac{\partial \Theta}{\partial z} = \frac{1}{\delta^2 \text{Pr Re}} \frac{\partial^2 \Theta}{\partial z^2}. \tag{17}$$

Dimensional analysis yields $\delta^2 \sim (\text{Re}^{-1})$, $\delta^* = \delta L^* = (\nu^*/\Omega_D^*)^{1/2}$, $\text{Pr} = c_p^* \rho^* / k^*$.

In this case it can be assumed that the pressure above the boundary layer is constant across the boundary layer thickness. The pressure distribution in the fluid rotating at a constant angular Ω can be obtained using $\partial P / \partial r = \Omega r / \Omega_D$.

For von Kármán flow, $\partial P / \partial r = 0$, this set of equations leads to

$$2U + \overline{W} = 0, \tag{18}$$

$$U^2 + W\overline{U} - (V+1)^2 + \beta\Theta - \overline{\overline{U}} = 0, \tag{19}$$

$$2U(V+1) + W\overline{V} + \beta\Theta - \overline{\overline{V}} = 0, \tag{20}$$

$$W\overline{W} + \overline{P} - \overline{\overline{W}} = 0, \tag{21}$$

$$\text{Pr}\, W\overline{\Theta} - \overline{\overline{\Theta}} = 0, \tag{22}$$

where the prime denotes differentiation with respect to the z direction.

Equations of von Kármán flow can then be solved numerically with the following boundary conditions:

$$U(0) = V(0) = W(0) = 0, \quad \Theta(0) = \Theta_2,$$
$$U(z \to \infty) = 0, \quad V(z \to \infty) = 1, \quad \Theta(z \to \infty) = \Theta_1. \tag{23}$$

Figure 3 shows the velocity distribution of self-similar solutions for $B = (\Theta_2^* - \Theta_1^*)/\Theta_1^* = [-0.05, 0, 0.05]$ in the von Kármán boundary layer. Please note that, in the definition of the thermal Rossby number B, the numerator represents the temperature difference between the rotating side and the fluid. Therefore, the current B in the BEK model for the von Kármán boundary layer is negative, indicating that the temperature on the rotating side is lower than that of the fluid. This is in contrast with the subsequent large-eddy simulation (LES) where B is defined as positive, indicating that the rotating side has a lower temperature than the fluid.

Due to the challenge of achieving convergence caused by a large thermal Rossby number B in the exact numerical solution, we carefully selected three specific conditions: $B = -0.05$, $B = 0$, and $B = 0.05$. These chosen conditions effectively reflect the influence of centrifugal buoyancy on the exact numerical solution for a single disk.

For values of B less than zero and greater than zero, the centrifugal buoyancy force acts outward and inward along the radial direction, respectively. As the thermal Rossby number B increases, indicating a rise in temperature on the disk, the magnitude of the centrifugal buoyancy force acting outward along the radial direction decreases.
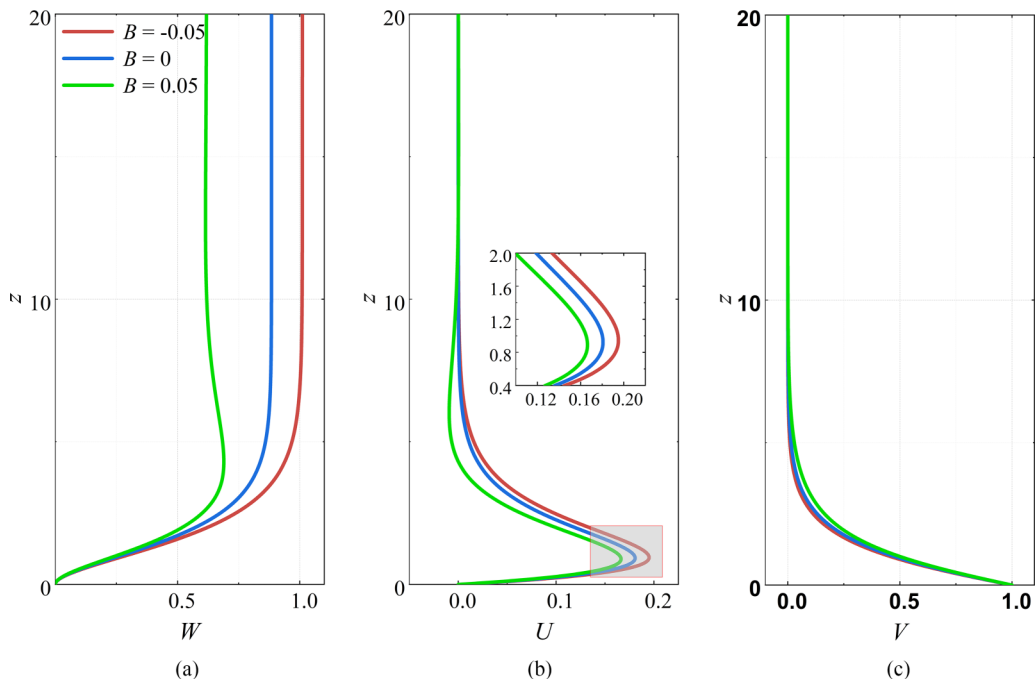
FIG. 3. Self-similar velocity profiles of the von Kármán flow for the case $B = -0.05$, 0, and 0.05. (a) Axial velocity W, (b) radial velocity U, and (c) azimuthal velocity V. The red line is for $B = -0.05$, the blue line is for $B = 0$, and the green line is for $B = 0.05$.

In the case of the von Kármán flow, when B is less than zero, the centrifugal buoyancy force in the radial outward direction causes a significant increase in radial velocity within the boundary layer. Following the law of mass conservation in the meridional (r, z) semiplane, an increase in radial velocity naturally leads to an increase in axial velocity. Therefore, when the direction of the centrifugal buoyancy force aligns with the radial velocity, it results in an increase in both radial and axial velocities. However, due to the significant centrifugal force in the base flow, the von Kármán boundary layer is sensitive to changes in centrifugal buoyancy. This implies that variations in the centrifugal buoyancy force have a more pronounced effect on the mean flow in the von Kármán boundary layer.

The above conclusion demonstrates that, as the thermal Rossby number B varies, the base flow exhibits consistent changes. Therefore, in order to conduct more effective large-eddy simulations, B values greater than zero are selected in the subsequent analysis.

IV. EFFECT OF THERMAL ROSSBY NUMBER ON VON KÁRMÁN LAYER IN A ROTOR-STATOR CAVITY

In the high Reynolds number flow with $\text{Re} = 4 \times 10^5$, the stator side has already transitioned to a fully turbulent flow, while the boundary layer on the rotor side exists in a state of coexistence between laminar, transition, and turbulence [20,24,40]. Due to the larger thermal Rossby number B, the convergence becomes more difficult. Therefore, three parameters, $B = 0$, 0.05, and 0.1, have been chosen for the current operating condition.

Figure 4 presents the averaged flow characteristics inside the cavity. Specifically, Fig. 4(a) illustrates the axial distribution of radial velocity U at $\widetilde{r} = 0.5$ [$\widetilde{r} = (r - a)/(b - a)$]. In the study, the influence of viscous forces is more pronounced in the current operating condition, while the impact of centrifugal forces is relatively weaker. Nevertheless, centrifugal forces still lead to an
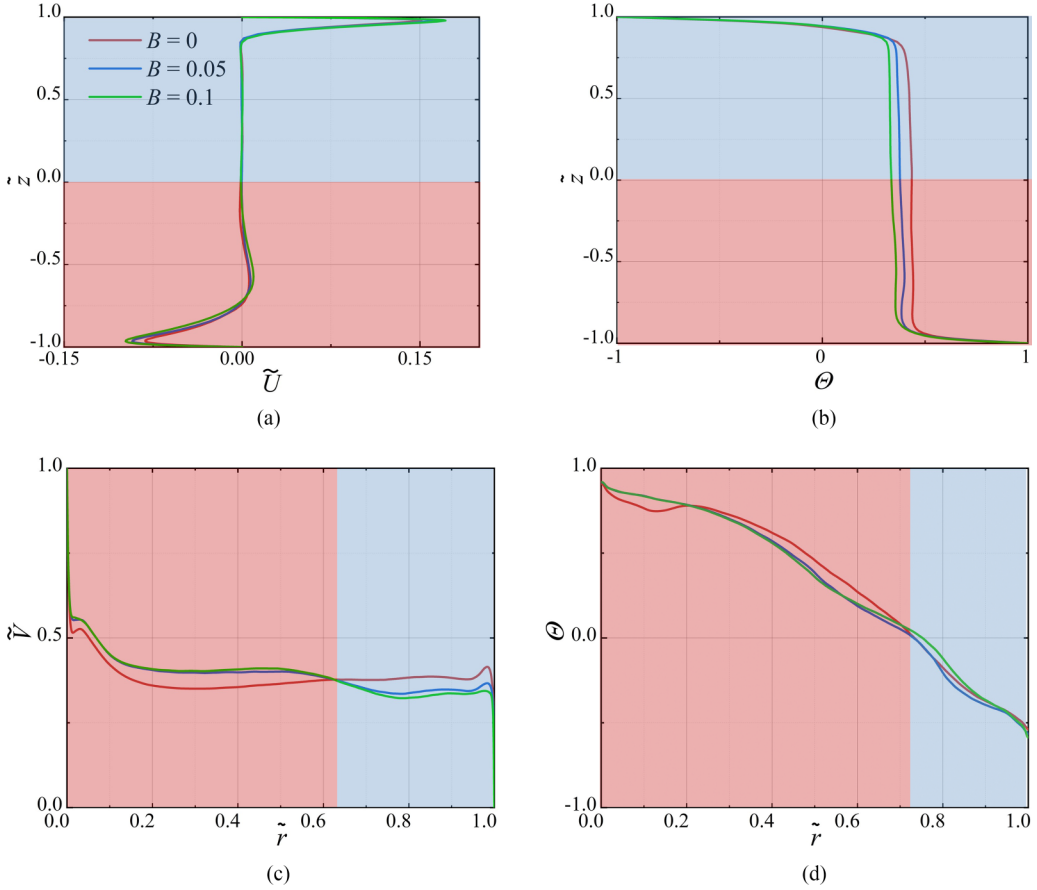
FIG. 4. Mean velocity and temperature profiles of the flow in the rotor-stator cavity at $Re = 4 \times 10^5$. (a) Dimensionless average radial velocity $\widetilde{U}[\widetilde{U} = U/(\Omega_D r)]$ at $\widetilde{r} = 0.5$; (b) dimensionless average temperature Θ at $\widetilde{r} = 0.5$; (c) dimensionless average azimuthal velocity $\widetilde{V}[\widetilde{V} = V/(\Omega_D r)]$ at $z = 0$; (d) dimensionless average temperature Θ at $z = 0$. The red line is for $B = 0$, the blue line is for $B = 0.05$, and the green line is for $B = 0.1$.

increase in the dimensionless radial velocity within the two boundary layers. This indicates that even under the current condition, centrifugal forces still exert a certain influence on the flow. In Fig. 4(b), a distinct pattern can be observed in the temperature distribution at $\widetilde{r} = 0.5$. As B increases, the temperature gradients within the boundary layers on the stator side and rotor side become larger and smaller, respectively. Furthermore, in the core regions within the two boundary layers, the temperature remains relatively constant. In Fig. 4(c), the radial distribution of nondimensional circumferential velocity at the midsection ($z = 0$) of the two disks is presented. The nondimensional circumferential velocity increases with an increase in B at the lower radii and decreases with an increase in B at the higher radii. In Fig. 4(d), the radial distribution of temperature at the midsection ($z = 0$) of the two disks is shown. There are some differences in temperature near the hub at the lower radii. This discrepancy may be attributed to the introduction of centrifugal forces, causing significant changes in the flow near the hub. However, as this paper primarily focuses on the impact of centrifugal forces on the boundary layer of the disk, the discussion regarding the temperature discrepancies near the hub at the lower radii is considered beyond the scope of the present study.

Figure 5 presents a temperature contour plot within the boundary layer on the rotor side, offering a vivid depiction of the distinct characteristics of laminar flow, transition, and turbulence on the disk
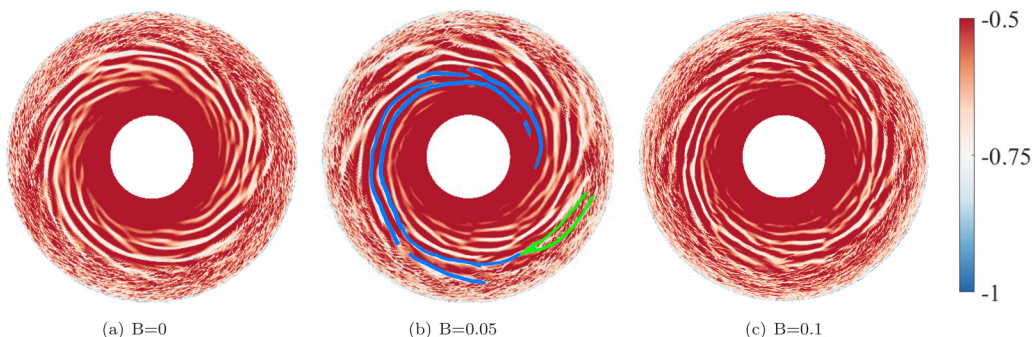
FIG. 5. Contour plot of instantaneous dimensionless temperature Θ at $z = 0.98$ for $\mathrm{Re} = 4 \times 10^5$.

surface. It is important to note that the unstable spiral waves observed in the transition region exhibit an opposite tilt direction compared with those on the stator side. However, due to the presence of bifurcation and fragmentation effects, accurately determining the number of spiral waves becomes challenging.

At higher radial positions, the spiral waves diminish, and only chaotic and irregular turbulent features are observed. Qualitatively, an increase in B amplifies the bifurcation effect of the spiral waves. Some spiral waves tend to prematurely fracture, leaving behind cone-shaped turbulent patches, as indicated by the green line region in Fig. 5(b). This phenomenon highlights the heightened instability of the boundary layer on the rotor side as centrifugal forces strengthen. The transition region progressively shifts towards lower radii, and the onset of turbulence occurs at relatively lower radii.

To quantitatively investigate the radial changes in the flow state of the rotating-disk boundary layer, we adopted the methodology outlined by Imayama *et al.* [41]. Specifically, at $z = 0.98$, we examined the radial distribution of the dimensionless root mean squared velocity, denoted V_{rms}. This parameter, defined as $V_{\mathrm{rms}} = [\overline{VV} - (\overline{V})^2]^{1/2}/(\Omega_D r)$, captures the fluctuations in velocity within the boundary layer.

Figure 6(a) demonstrates that the disturbances induced by the hub lead to significant circumferential velocity fluctuations, as indicated by the non-negligible values of the root mean square (V_{rms}) at lower radii. The x axis represents the dimensionless radial position $\widetilde{r}$. However, as the distance from the hub increases, the V_{rms} gradually decreases, signifying a progressive stabilization of the

FIG. 6. (a) Azimuthal fluctuation velocity V_{rms}, (b) growth rates $-\alpha_{\mathrm{i}}$ at $z = 0.98$ for $\mathrm{Re} = 4 \times 10^5$. The red line is for $B = 0$, the blue line is for $B = 0.05$, and the green line is for $B = 0.1$.
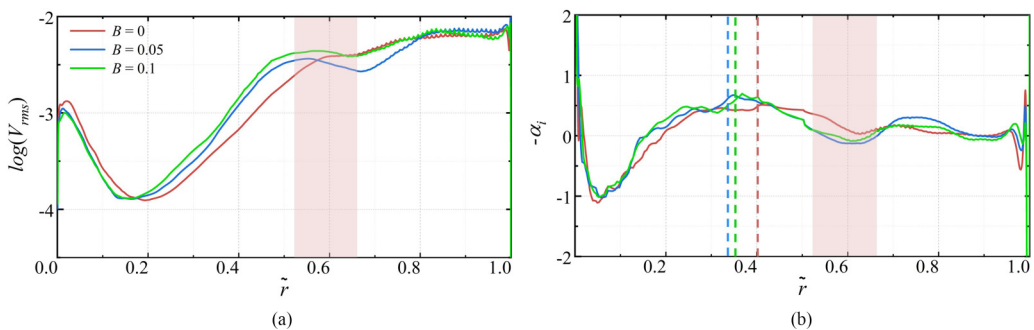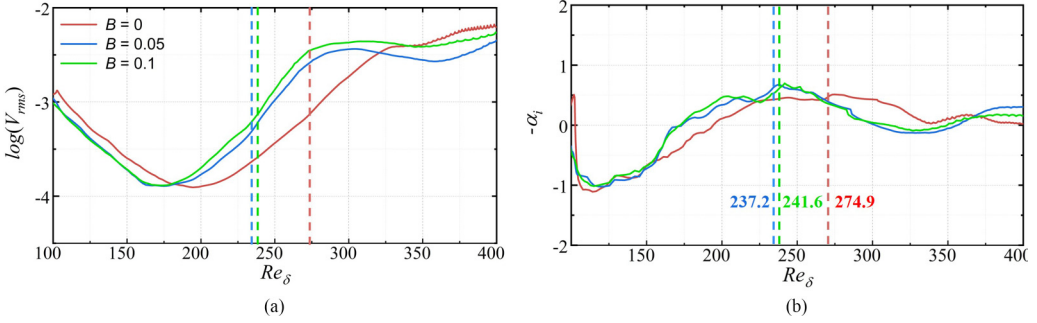
FIG. 7. (a) Azimuthal fluctuation velocity V_{rms}, (b) growth rates $-\alpha_i$ at $z = 0.98$ for $Re = 4 \times 10^5$. The red line is for $B = 0$, the blue line is for $B = 0.05$, and the green line is for $B = 0.1$. The x axis represents local Reynolds Re_δ, which is defined according to Eq. (1).

flow. Continuing further in the radial direction, the V_{rms} value reaches a minimum. Subsequently, with the emergence of spiral waves, the V_{rms} value experiences a rapid increase. In the case of $B = 0$, when approaching the radial position where the spiral waves break, the V_{rms} value does not exhibit a decrease as observed during the rupture of individual rotating disk's spiral waves [28,41]. Instead, it gradually increases with the radial position. This behavior can be attributed to the intensification of disturbances at higher radii caused by the presence of the shroud. In the case of $B = 0$, where the position of spiral wave breakage is closer to higher radii, the V_{rms} value does not decrease but rather shows a slow increase. This can be attributed to the exacerbation of disturbances at higher radii by the shroud. Furthermore, the presence of the shroud also contributes to a sharp increase in the V_{rms} value in the outermost region. This finding is consistent with the observations of Yim *et al.* [20] and suggests that the shroud plays a role in amplifying turbulence in the outermost region. In the presence of centrifugal forces, the spiral waves tend to break earlier compared with the case of $B = 0$. The rupture of spiral waves leads to a slight decrease in the V_{rms} value, as indicated by the prominent feature represented by the shades of pink in Fig. 6. This observation is consistent with the findings reported by Imayama *et al.* [28,41]. Subsequently, the presence of the shroud induces disturbances, leading to a gradual increase in the V_{rms} value. As the region predominantly influenced by the shroud is approached, the curves for all three cases nearly coincide, indicating a convergence in the behavior of V_{rms}.

By analyzing the amplitudes of V_{rms}, it is possible to determine the radial growth rate, denoted $-\alpha_i$, assuming an exponential decay of the form $V_{rms} \sim \exp(-\alpha_i r)$, as depicted in Fig. 6(b). To ensure data consistency, a moving average method with a window size of $n = 5$ was applied for curve fitting. This approach helps to smooth out the data by calculating the average of each point and its neighboring four points, providing a more representative trend. The growth rate starts to decrease after reaching its maximum value. This decrease in the growth rate is commonly attributed to nonlinear effects [41].

All the analyses presented thus far have been based on the local dimensionless radius $\tilde{r}$. However, in order to facilitate a more meaningful interpretation of the flow characteristics and to relate them to existing literature, in Fig. 7, the values of $\tilde{r}$ have been converted into Re_δ using the precise definitions provided in Eq. (1).

From Fig. 7(b), it is evident that, when $B = 0$, the onset of nonlinear effects occurs at $Re_\delta = 274.9$. In contrast, when considering the rotor-stator cavity without a hub, this value is 298.2 [20], while for a single rotating disk, it is 507. This discrepancy can be attributed to the additional disturbances introduced by the hub, which lead to the premature occurrence of nonlinear effects. However, the introduction of centrifugal buoyancy forces shifts the onset of nonlinear effects to lower Reynolds numbers. Specifically, for $B = 0.05$ and $B = 0.1$, the onset of nonlinear effects is triggered at approximately $Re_\delta \approx 240$. This indicates that the presence of centrifugal buoyancy
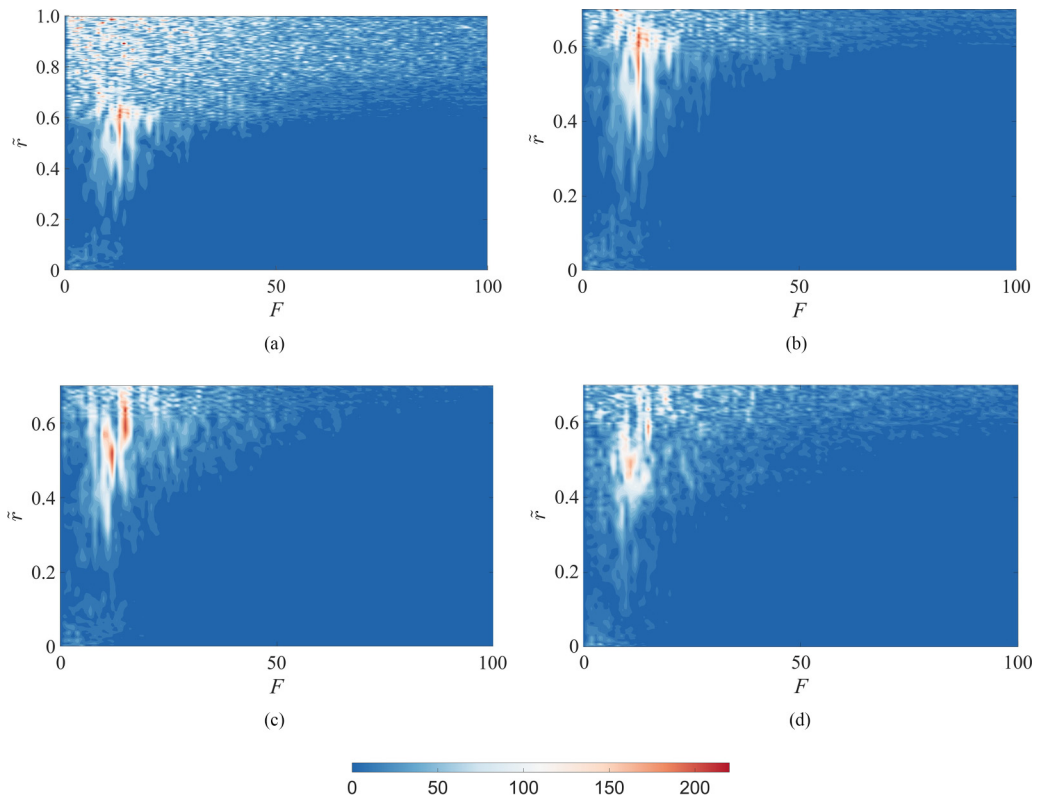
FIG. 8. Frequency-radial contour plot at $(z = 0.98, \theta = 0)$ for $Re = 4 \times 10^5$, where the color represents the magnitude of each frequency obtained from the FFT transformation. (a) $B = 0(0 < \tilde{r} < 1)$, (b) $B = 0(0 < \tilde{r} < 0.7)$, (c) $B = 0.05(0 < \tilde{r} < 0.7)$, (d) $B = 0.1(0 < \tilde{r} < 0.7)$.

forces accelerates the onset of nonlinear phenomena, leading to a transition to more complex flow behavior at lower Reynolds numbers compared with the case without centrifugal buoyancy forces. Importantly, as the centrifugal buoyancy force continues to increase, the critical Reynolds number does not decrease further. This indicates that there exists a minimum value for the critical Reynolds number in the von Kármán boundary layer beyond which an increase in centrifugal buoyancy force does not reduce the critical Reynolds number any further.

Through the preceding discussion, we have elucidated the impact of centrifugal buoyancy on the transition region. However, we have not delved into the specific changes in the spiral waves and their influence on the transition region. To address this, we conducted a fast Fourier transform (FFT) analysis along the radial position at $z = 0.98$ and $\theta = 0$ to investigate this phenomenon in more detail. The results are depicted in Fig. 8, where the color indicates the magnitude of the corresponding frequency amplitude.

Figure 8 depicts the spectrogram of the entire radial range under the $B = 0$ condition. Near the frequency F $[F = F^* 2 \pi /(\Omega_D^*)]$ approximately equal to 13, a noteworthy high-amplitude region emerges within positions where $0.4 < \tilde{r} < 0.6$. This particular frequency and amplitude result primarily from the presence of spiral waves. As the radial position increases, and the flow undergoes a transition to fully turbulent, the amplification of high-frequency regions experiences a rapid increment but tends to be uniformly distributed without a distinct dominant amplitude, as shown by the red solid line in the Fig. 8(a). The high-frequency region of Fig. 8(a) exhibits a clear boundary near the radius $\tilde{r} = 0.6$. This aligns precisely with a characteristic of turbulence. To reduce the influence of fully turbulent regions with consistent attributes at higher radii on flow analysis,
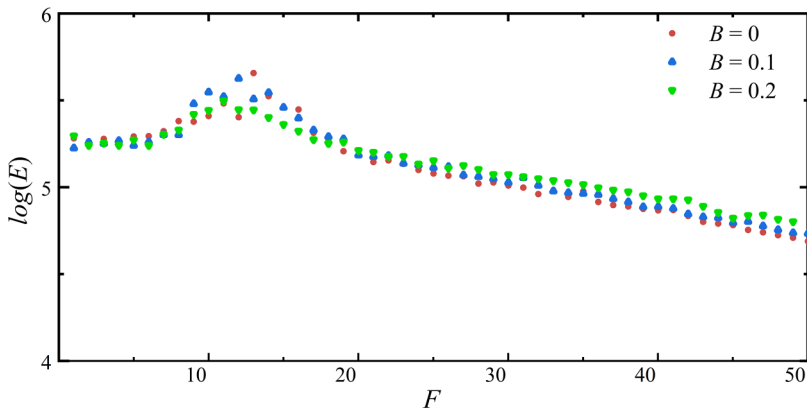
FIG. 9. Modes and energy obtained from dynamic mode decomposition at $z = 0.98$ for $\text{Re} = 4 \times 10^5$. F/F_0 represents the mode normalized by the rotational frequency of the disk. E represents the energy corresponding to the mode. The red dot is for $B = 0$, the blue triangle is for $B = 0.05$, the green inverted triangle is for $B = 0.1$.

Figs. 8(b)–8(d) display only the intercepted spectral cloud images within $0 < \tilde{r} < 0.7$, representing the three operating conditions of $B = 0$, 0.05, and 0.1, respectively. In the case of $B = 0.05$, two distinctive regions of high amplitude with different dominant frequencies are observed within $0.3 < \tilde{r} < 0.6$. Upon closer examination, it becomes evident that these two frequencies overlap in the radial direction, indicating that the presence of different modes is induced by the branching or breaking of the spiral waves in this specific region. This phenomenon of bifurcation on a single rotor disk aligns with Fig. 12 of the study by Imayama *et al.* [41]. When $B = 0.1$, the radial extent occupied by the dominant frequencies begins to diminish at $\tilde{r} = 0.5$, and another mode dominated by a different frequency emerges at subsequent positions. It can be inferred that the introduction of centrifugal forces leads to a faster branching and decay of spiral wave structures in the transition zone, as reflected in the frequency spectrum.

Figure 9 shows the modes and the energy distribution diagrams corresponding to the modes obtained by DMD decomposition of 6280 time series within one turntable period on the $z = 0.98$ surface. From $B = 0$ to $B = 0.1$, the modal energy with the highest energy gradually decreases, and the corresponding frequency becomes smaller. However, the energy corresponding to almost all high-frequency modes increases. This reflects the premature breakdown of the dominant mode, leading to the transfer of its energy to all high-frequency modes.

V. THE LOCAL LINEAR STABILITY ANALYSIS

In this section, we refer to the fourth-order Orr-Sommerfeld equations as outlined by Lingwood [9]. Then extract the velocity profiles from the current numerical simulation results and use them in the linear stability analysis.

The specific derivation of the equations can be found in Lingwood [9]; however, for brevity, we provide the expression of the fourth-order Orr-Sommerfeld equations here without delving into the detailed derivation:

$$[i(D^2 - \gamma^2)^2 + R(\alpha U + \overline{\beta}V - \omega)(D^2 - \gamma^2) - R(\alpha D^2 U + \overline{\beta}D^2 V)]X = 0. \tag{24}$$
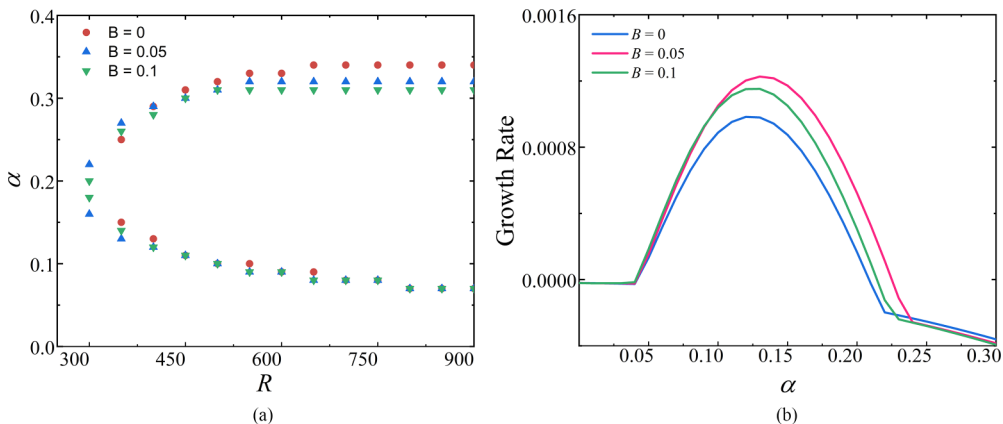
FIG. 10. (a) Neutral ($\omega_i = 0$, $\alpha_i = 0$) stability diagrams, calculated from the fourth-order Orr-Sommerfeld equation at $\overline{\beta} = 0.0467$. (b) The relationship between the local temporal growth rate ω_i and the radial wave number α for the azimuthal wave number $\overline{\beta} = 0.049$. Red is for $B = 0$, blue is for $B = 0.05$, green is for $B = 0.1$.

In the context of the fourth-order Orr-Sommerfeld equations, the symbols have the following meanings: ω represents the frequency of the disturbance in the rotating frame, $R = r/\delta$ represents the Reynolds number which is based on the viscous length. $\overline{\beta}$ is the prescribed integer circumferential wave number ($\overline{\beta} = m/R$), m is the number of spiral waves, α is the radial wave number, and $\gamma^2 = \alpha^2 + \overline{\beta}^2$.

For the rotating-disk boundary layer, velocity profiles were selected at $\widetilde{r} = 0.5$, corresponding to a Reynolds number of $R = 406$. The objective of this selection was to investigate the stability characteristics in the unstable region of the boundary layer under temporal modes.

However, it is important to note that there is a difference in length scales between the current Orr-Sommerfeld equations, where the z direction is scaled by the viscous length scale δ, and the numerical simulation, where the length scale is half the distance between the disks. Therefore, to apply the velocity profiles from the numerical simulation to the current equations properly, a suitable stretching transformation is required:

$$\frac{\partial U}{\partial \delta} = \frac{\partial U}{\partial h}\frac{h}{r}\frac{r}{\delta} = \frac{\partial U}{\partial h}\frac{h}{r}R. \tag{25}$$

Due to the presence of azimuthal velocity in the core region of the rotor-stator cavity, the Reynolds number R should be based on the viscous length scale and rotating velocity of fluid away from the disk. So here R should be replaced with Re_δ.

Figure 10(a) illustrates the results of the stability analysis on the rotating side. The thermal Rossby number only affects the upper branch of the neutral curve. However, in contrast, as the thermal Rossby number increases, the opening of the upper branch of the neutral curve becomes smaller. The results in Fig. 10(b) demonstrate that when the thermal Rossby number is greater than zero, any disturbance at the local level increases with time, indicating that the flow is unstable and will develop into turbulence. Upon closer examination, within the range of α from 0.04 to 0.1, the growth rates corresponding to $B = 0.05$ and $B = 0.1$ are nearly identical, consistent with the results from the numerical simulation. This suggests that for these two operating conditions, the critical

Reynolds number for convective instability has reached its minimum value. For larger values of α, the growth rate at $B = 0.05$ is higher than at $B = 0.1$, which is consistent with the instability reflected in the azimuthal fluctuation velocity V_{rms} in Figs. 6(a) and 7(a). However, the variation in V_{rms} between $B = 0.05$ and $B = 0.1$ is small, while the current variation is significant. Regarding this issue, we believe that linear stability analysis overlooks specific factors such as radial constraints that are unique to the rotor-stator cavity. Therefore, the results of linear stability analysis should be considered as a reference, while the outcomes obtained from large-eddy simulations provide a more accurate basis for analysis.

VI. SUMMARY AND CONCLUDING REMARKS

This study investigates the laminar-transition-turbulent process of incompressible rotating-disk boundary layers in a centrifugal buoyancy-driven cavity using theoretical analysis and large-eddy simulation. The typical transition Reynolds numbers, $\text{Re} = 4 \times 10^5$ was selected based on existing literature. In the numerical simulations, the density variations caused by temperature changes were simulated in a rotating cylindrical coordinate system using the Boussinesq assumption. The main findings of this study can be summarized as follows:

(i) As the Reynolds number increases, the influence of viscous shear stress on the flow in the rotor-stator cavity becomes more significant, while the effect of temperature-induced centrifugal buoyancy weakens. Therefore, the changes in the dimensionless radial and azimuthal velocities caused by centrifugal buoyancy at the current Reynolds number are smaller.

(ii). Despite the small temperature difference and resulting small changes in dimensionless velocities in the current case, our LES revealed that the stability of the rotating-disk boundary layer on the rotating disk is still significantly affected. Specifically, when the temperature on the rotating side is lower, the rotating-disk boundary layer experiences an early breakdown of Type I spiral waves mode caused by crossflow instability, leading to a decrease in the critical Reynolds number for transition to turbulence.

(iii) It seems that there is a minimum value for the critical Reynolds number when the flow transitions to turbulence on the rotating side. In the current simulation, it is observed that as B increases, the critical Reynolds number reaches a minimum value and does not decrease further. Specifically, the minimum critical Reynolds number at which nonlinear effects occur is approximately $\text{Re}_\delta \approx 240$.

Based on the research, we have identified the unique influence of temperature difference on rotating-disk boundary layers. Although relatively simple models were used, the qualitative findings and the role of temperature-induced centrifugal buoyancy in this typy of boundary layers can be extended to similar flow conditions.

APPENDIX : NOMENCLATURE

Table II lists the nomenclature used in this paper.

TABLE II. Nomenclature of all parameter symbols appearing in the paper.

a^*	Internal radii (dimensional)
a	Internal radii (a^*/h^*)
b^*	External radii (dimensional)
b	External radii (b^*/h^*)
B	Thermal Rossby number; $B = \beta^*(\Theta_2^* - \Theta_1^*)$
E	Energy corresponding to the mode in DMD
$F*$	Sampling point frequency (dimensional)
F	Sampling point dimensionless frequency; $F = F^* 2\pi/(\Omega_D^*)$
h^*	Half the spacing between the disks (dimensional)
L	Aspect ratio; $L = (b^* - a^*)/2h^*$
$\boldsymbol{N}(\boldsymbol{u})$	Nonlinear term
N_z, N_r, N_θ	Axial, radial and azimuthal degrees of freedom
P	Pressure
r	Local radius (r^*/h^*)
$\widetilde{r}$	Local radius; $\widetilde{r} = (r - a)/(b - a)$
Ro	Rossby number; $Ro(r) = \Delta\Omega(r)/\Omega(r)$
Re_δ	Local Reynolds numbers based on viscous length δ and Rossby number Ro; $\mathrm{Re}_\delta = R\mathrm{Ro}$
R	Reynolds number based on viscous length δ; $R = r/\delta$
Re	Global Reynolds numbers; $\mathrm{Re} = \Omega_D b^2/\nu$
Re_r	Local Reynolds numbers; $\mathrm{Re} = \Omega_D r^2/\nu$
R_m	Curvature parameter; $R_m = (b^* + a^*)/(b^* - a^*)$
$(\boldsymbol{u}\cdot\nabla\boldsymbol{u} + \nabla\cdot\boldsymbol{uu})/2$	Nonlinear terms in skew-symmetric form
V_{rms}	Root mean square of the radial velocity; $V_{\mathrm{rms}} = [\overline{VV} - (\overline{V})^2]^{1/2}/(\Omega_D r)$
$\overline{V}$	Time and circumferentially averaged radial velocity V
W^*, U^*, V^*	Velocity of axial, radial and azimuthal direction (dimensional)
W, U, V	Dimensionless velocity of axial, radial and azimuthal direction; $(W, U, V) = (W^*, U^*, V^*)/(\Omega_D^* h^*)$
$\widetilde{W}, \widetilde{U}, \widetilde{V}$	Dimensionless velocity of axial, radial and azimuthal direction; $(\widetilde{W}, \widetilde{U}, \widetilde{V}) = (W, U, V)/(\Omega_D r)$
z	Dimensionless local axial based on viscous length (z^*/δ^*)
$\widetilde{z}$	Dimensionless local axial; $\widetilde{z} = z^*/h^*$
$\alpha, \overline{\beta}$	Radial and azimuthal wave numbers
α_E, β_E	Control parameters of ν_E
β^*	Thermal expansion coefficient; $\beta^* = 1/\Theta_{\mathrm{ref}}^*$
β	Dimensionless thermal expansion coefficient; $\beta = B/(\Theta_2 - \Theta_1)$
Ω_D^*	Angular velocity of the rotating disk (dimensional)
Ω	Dimensionless angular velocity of the disk
$\Omega_F(r)$	Rotational velocity of the fluid away from the disk boundary layer
Θ^*	Temperature (dimensional)
Θ_1^*, Θ_2^*	Temperature of rotor and stator (dimensional)
Θ_{ref}^*	Reference temperature in Boussinesq approximation; $\Theta_{\mathrm{ref}}^* = (\Theta_2^* + \Theta_1^*)/2$
Θ	Dimensionless temperature. $\Theta = (2\Theta^* - \Theta_2^* - \Theta_1^*)/(\Theta_2^* - \Theta_1^*)$
Θ_1, Θ_2	Dimensionless temperature of rotor and stator
δ	Viscous length. $\delta = \sqrt{\nu/\Omega_D}$
$\Delta\Omega(r)$	The difference in rotational velocity of the fluid away from the disk boundary layer with the rotor
ν_E, ν_Θ	Scalars denoting the turbulent eddy viscosity and turbulent diffusivity in LES-EVM
$-\alpha_r$	Radial growth rate

[1] T. v. Kármán, Über laminare und turbulente reibung, Z. Angew. Math. Mech. **1**, 233 (1921).

[2] P. H. Alfredsson, K. Kato, and R. Lingwood, Flows over rotating disks and cones, Annu. Rev. Fluid Mech. **56**, 45 (2024).

[3] G. K. Batchelor, Note on a class of solutions of the Navier-Stokes equations representing steady rotationally-symmetric flow, Q. J. Mech. Appl. Math. **4**, 29 (1951).

[4] B. Launder, S. Poncet, and E. Serre, Laminar, transitional, and turbulent flows in rotor-stator cavities, Annu. Rev. Fluid Mech. **42**, 229 (2010).

[5] D. Martinand, E. Serre, and B. Viaud, Instabilities and routes to turbulence in rotating disc boundary layers and cavities, Philos. Trans. R. Soc. London A **381**, 20220135 (2023).

[6] R. Kobayashi, Y. Kohama, and C. Takamadate, Spiral vortices in boundary layer transition regime on a rotating disk, Acta Mech. **35**, 71 (1980).

[7] M. R. Malik, S. P. Wilkinson, and S. A. Orszag, Instability and transition in rotating disk flow, AIAA J. **19**, 1131 (1981).

[8] Y. Kohama, Study on boundary layer transition of a rotating disk, Acta Mech. **50**, 193 (1984).

[9] R. J. Lingwood, Absolute instability of the boundary layer on a rotating disk, J. Fluid Mech. **299**, 17 (1995).

[10] R. J. Lingwood, Absolute instability of the Ekman layer and related rotating flows, J. Fluid Mech. **331**, 405 (1997).

[11] R. Lingwood, An experimental study of absolute instability of the rotating-disk boundary-layer flow, J. Fluid Mech. **314**, 373 (1996).

[12] B. Pier, Finite-amplitude crossflow vortices, secondary instability and transition in the rotating-disk boundary layer, J. Fluid Mech. **487**, 315 (2003).

[13] C. Davies and P. W. Carpenter, Global behaviour corresponding to the absolute instability of the rotating-disc boundary layer, J. Fluid Mech. **486**, 287 (2003).

[14] C. Davies, C. Thomas, and P. W. Carpenter, Global stability of the rotating-disk boundary layer, J. Eng. Math. **57**, 219 (2007).

[15] H. Othman and T. Corke, Experimental investigation of absolute instability of a rotating-disk boundary layer, J. Fluid Mech. **565**, 63 (2006).

[16] E. Appelquist, P. Schlatter, P. H. Alfredsson, and R. J. Lingwood, On the global nonlinear instability of the rotating-disk flow over a finite domain, J. Fluid Mech. **803**, 332 (2016).

[17] K. Lee, Y. Nishio, S. Izawa, and Y. Fukunishi, The effect of downstream turbulent region on the spiral vortex structures of a rotating-disk flow, J. Fluid Mech. **844**, 274 (2018).

[18] B. Viaud, E. Serre, and J.-M. Chomaz, The elephant mode between two rotating disks, J. Fluid Mech. **598**, 451 (2008).

[19] B. Viaud, E. Serre, and J.-M. Chomaz, Transition to turbulence through steep global-modes cascade in an open rotating cavity, J. Fluid Mech. **688**, 493 (2011).

[20] E. Yim, J.-M. Chomaz, D. Martinand, and E. Serre, Transition to turbulence in the rotating disk boundary layer of a rotor–stator cavity, J. Fluid Mech. **848**, 631 (2018).

[21] G. Ahlers, Critical phenomena at low temperature, Rev. Mod. Phys. **52**, 489 (1980).

[22] B.-F. Wang, Q. Zhou, and C. Sun, Vibration-induced boundary-layer destabilization achieves massive heat-transport enhancement, Sci. Adv. **6**, eaaz8239 (2020).

[23] X.-L. Guo, J.-Z. Wu, B.-F. Wang, Q. Zhou, and K. L. Chong, Flow structure transition in thermal vibrational convection, J. Fluid Mech. **974**, A29 (2023).

[24] É. Séverac, S. Poncet, É. Serre, and M.-P. Chauve, Large eddy simulation and measurements of turbulent enclosed rotor-stator flows, Phys. Fluids **19**, 085113 (2007).

[25] S. Poncet and É. Serre, High-order LES of turbulent heat transfer in a rotor–stator cavity, Int. J. Heat Fluid Flow **30**, 590 (2009).

[26] M. Queguineur, T. Bridel-Bertomeu, L. Y. Gicquel, and G. Staffelbach, Large eddy simulations and global stability analyses of an annular and cylindrical rotor/stator cavity limit cycles, Phys. Fluids **31**, 104109 (2019).

[27] Q. Du, Y. Xie, Z. Wang, X. Jiang, and L. Xie, An entropy viscosity method for large eddy simulation of turbulent thermal flow in a rotor–stator cavity, Phys. Fluids **35**, 035126 (2023).

[28] S. Imayama, P. H. Alfredsson, and R. J. Lingwood, An experimental study of edge effects on rotating-disk transition, J. Fluid Mech. **716**, 638 (2013).

[29] E. Appelquist, P. Schlatter, P. H. Alfredsson, and R. Lingwood, Transition to turbulence in the rotating-disk boundary-layer flow with stationary vortices, J. Fluid Mech. **836**, 43 (2018).

[30] N. Peres, S. Poncet, and E. Serre, A 3D pseudospectral method for cylindrical coordinates. application to the simulations of rotating cavity flows, J. Comput. Phys. **231**, 6290 (2012).

[31] E. Serre, E. C. Del Arco, and P. Bontoux, Annular and spiral patterns in flows between rotating and stationary discs, J. Fluid Mech. **434**, 65 (2001).

[32] J.-L. Guermond, On the use of the notion of suitable weak solutions in CFD, Int. J. Numer. Methods Fluids **57**, 1153 (2008).

[33] J.-L. Guermond, R. Pasquetti, and B. Popov, From suitable weak solutions to entropy viscosity, in *Quality and Reliability of Large-Eddy Simulations II* (Springer, 2011), pp. 373–390.

[34] J.-L. Guermond, A. Larios, and T. Thompson, Validation of an entropy-viscosity model for large eddy simulation, in *Direct and Large-Eddy Simulation IX* (Springer, 2015), pp. 43–48.

[35] Z. Wang, M. S. Triantafyllou, Y. Constantinides, and G. E. Karniadakis, An entropy-viscosity large eddy simulation study of turbulent flow in a flexible pipe, J. Fluid Mech. **859**, 691 (2019).

[36] H. M. Blackburn, D. Lee, T. Albrecht, and J. Singh, Semtex: A spectral element–Fourier solver for the incompressible Navier–Stokes equations in cylindrical or cartesian coordinates, Comput. Phys. Commun. **245**, 106804 (2019).

[37] C. Chicchiero, A. Segalini, and S. Camarri, Triple-deck analysis of the steady flow over a rotating disk with surface roughness, Phys. Rev. Fluids **6**, 014103 (2021).

[38] C. Thomas, S. O. Stephen, and C. Davies, Effects of partial slip on the local-global linear stability of the infinite rotating disk boundary layer, Phys. Fluids **32**, 074105 (2020).

[39] C. Thomas and C. Davies, An adjoint approach for computing the receptivity of the rotating disc boundary layer to surface roughness, J. Fluid Mech. **926**, A16 (2021).

[40] S. Makino, M. Inagaki, and M. Nakagawa, Laminar-turbulence transition over the rotor disk in an enclosed rotor-stator cavity, Flow, Turbul. Combust. **95**, 399 (2015).

[41] S. Imayama, P. H. Alfredsson, and R. J. Lingwood, On the laminar–turbulent transition of the rotating-disk flow: The role of absolute instability, J. Fluid Mech. **745**, 132 (2014).